Solar Phys
DOI 10.1007/s11207-013-0314-8

Kinematics of Interacting ICMEs and Related Forbush Decrease: Case Study

D. Maričić · B. Vršnak · M. Dumbović · T. Žic · D. Roša · D. Hržina · S. Lulić · I. Romštajn · I. Bušić · K. Salamon · M. Temmer · T. Rollett · A. Veronig · N. Bostanjyan · A. Chilingarian · B. Mailyan · K. Arakelyan · A. Hovhannisyan · N. Mujić

Received: 7 January 2013 / Accepted: 27 April 2013

Abstract We study heliospheric propagation and some space weather aspects of three Earth-directed interplanetary coronal mass ejections (ICMEs), successively launched from the active region AR 11158 in the period 13 – 15 February 2011. From the analysis of the ICME kinematics, morphological evolution, and *in situ* observations, we infer that the three ICMEs interacted on their way to Earth, arriving together at 1 AU as a single interplanetary disturbance. Detailed analysis of the *in situ* data reveals complex internal structure of the disturbance, where signatures of the three initially independent ICMEs could be recognized. The analysis also reveals compression and heating of the middle ICME, as well as ongoing magnetic reconnection between the leading and the middle ICME. We present evidence showing that the propagation of these two, initially slower ICMEs, was boosted by the fastest, third ICME. Finally, we employ the ground-based cosmic ray observations,

D. Maričić (✉) · D. Roša · D. Hržina · I. Romštajn · I. Bušić
Astronomical Observatory Zagreb, Opatička 22, 10000 Zagreb, Croatia
e-mail: darije.maricic@zg.htnet.hr

D. Roša
e-mail: drosa@zvjezdarnica.hr

D. Hržina
e-mail: dhrzina@zvjezdarnica.hr

I. Romštajn
e-mail: iromstajn@zvjezdarnica.hr

I. Bušić
e-mail: ibusic_zgb@yahoo.com

B. Vršnak · M. Dumbović · T. Žic
Faculty of Geodesy, Hvar Observatory, Kačićeva 26, 10000 Zagreb, Croatia

B. Vršnak
e-mail: bvrsnak@gmail.com

M. Dumbović
e-mail: mdumbovic@gmail.com

T. Žic
e-mail: tzic@geof.hr

Published online: 07 June 2013

to show that this complex disturbance produced a single cosmic ray event, *i.e.*, a simple Forbush decrease (FD). The results presented provide a better understanding of the ICME interactions and reveal effects that should be taken into account in forecasting of the arrival of such compound structures.

Keywords Cosmic rays · Interplanetary coronal mass ejections · Solar wind, disturbances

1. Introduction

Forbush decreases (FDs) are sudden, short-term depressions in the cosmic ray (CR) flux, which typically have a duration of a few days and a magnitude larger than the daily CR flux variations. They were first reported by Forbush (1937) and Hess and Demmelmair (1937). FDs are associated with solar activity (Simpson, 1954), as they are caused by short-term changes in the ambient solar wind (SW) and interplanetary magnetic field (IMF), associated with interplanetary coronal mass ejections (ICMEs) and corotating interaction regions

S. Lulić
Karlovac University of Applied Sciences, Trg J. J.Strossmayera 9, 47000 Karlovac, Croatia
e-mail: slulic@vuka.hr

M. Temmer · T. Rollett · A. Veronig
Kanzelhöhe Observatory-IGAM, Institute of Physics, University of Graz, Graz, Austria

M. Temmer
e-mail: manuela.temmer@uni-graz.at

T. Rollett
e-mail: tanja.rollett@uni-graz.at

A. Veronig
e-mail: asv@igam.uni-graz.at

N. Bostanjyan · A. Chilingarian · B. Mailyan · K. Arakelyan · A. Hovhannisyan
Cosmic Ray Division, Alikhanyan Physics Institute, Alikhanyan Brothers St. 2, Yerevan 36, Armenia

N. Bostanjyan
e-mail: nikolai@yerphi.am

A. Chilingarian
e-mail: chili@aragats.am

B. Mailyan
e-mail: bagrat_mailyan@yerphi.am

K. Arakelyan
e-mail: karen@crdlx5.yerphi.am

A. Hovhannisyan
e-mail: harmen@yerphi.am

K. Salamon
Institute of Physics, Bijenčka cesta 46, 10000 Zagreb, Croatia
e-mail: ksalamon@ifs.hr

N. Mujić
Faculty of Science, University of Sarajevo, Zmaja od Bosne 35, 71000 Sarajevo, Bosnia and Herzegovina
e-mail: nedim_mujic@bih.net.ba

(CIRs). ICMEs, *i.e.*, the interplanetary counterparts of coronal mass ejections (CMEs), are large-scale eruptions of unstable coronal magnetic structures, expelled into the heliosphere. On the other hand, CIRs are caused by high-speed solar-wind streams originating in low-latitude coronal holes. CR depressions caused by CIRs are typically more symmetric and shallower than those caused by ICMEs, which is especially prominent in the case of shock-associated ICMEs that cause the so-called two-step FD (see, *e.g.*, Lockwood, 1971; Cane, 2000; Richardson, 2004; Richardson and Cane, 2011).

On their way through the heliosphere, ICMEs can interact with CIRs and other ICMEs and form complex magnetoplasmatic structures. Such interactions occur frequently around the solar cycle maximum, when several CMEs can be launched within one day from the same source region. Usually, these complex structures contain enhanced southward magnetic field component, which is a key factor in generating geomagnetic storms (*e.g.*, Wang *et al.*, 2002). Furthermore, multiple ICMEs can lead to an enhanced reduction the incoming CR flux (*e.g.*, Dumbović *et al.*, 2012). Until recently, studies of CME interactions were limited only to the single-coronagraph observations of the upper corona (*e.g.*, Gopalswamy *et al.*, 2001). This situation has changed by the launch of the *Solar TErrestrial RElations Observatory* (STEREO; Kaiser *et al.*, 2008), which extended the range of the remote ICME observations to beyond 1 AU and provided measurements from multiple vantage points (*e.g.*, Liu *et al.*, 2012; Temmer *et al.*, 2012). A suite of remote sensing instruments of the *Sun Earth Connection Coronal and Heliospheric Investigation* (SECCHI; Thompson *et al.*, 2003; Howard *et al.*, 2008) can image ICMEs from their liftoff in the lower corona up to the Earth and beyond, providing observations of ICME interactions in the interplanetary space. Combining the remote observations with the *in situ* solar-wind measurements and the ground-based CR data can provide a better understanding of the ICME interactions and their effects.

The X2.2 solar flare that erupted on 15 February 2011 was the first X-class solar flare of sunspot cycle 24. It was associated with the Earth-directed CME and EUV wave (Schrijver *et al.*, 2011). The corresponding ICME caused disturbance in the ionosphere leading to telecommunication disruptions in the dayside regions (Kane, 2011b). On the other hand, the ICME lacked a substantial southward magnetic field component, so that it did not cause a significant geomagnetic storm (Kane, 2011a). This event was also associated with a substantial decrease in Galactic cosmic rays (GCR), *i.e.*, a Forbush decrease (Oh and Yi, 2012; Kane, 2012). An important aspect of the event was that the Sun exhibited an enhanced eruptive activity in the active region AR 11158 in the period 13 – 15 February 2011. The activity included multiple filament, flare, and CME eruptions, which led to a series of ICME–ICME interactions in the interplanetary space. The following analysis is focused on these interactions and the associated GCR-flux decrease, employing observations from STEREO and *Solar Dynamic Observatory* (SDO; Pesnell *et al.*, 2012) spacecraft, the *in situ* measurements at L1 and the ground-based CR recordings. For similar studies of ICME–ICME interaction see, *e.g.*, Liu *et al.* (2012), Shen *et al.* (2012), and Temmer *et al.* (2012).

2. Observations and Data Analysis

For the measurements of ICME kinematics we utilize the white-light and EUV images from STEREO-A and B instrument suite. The two spacecraft are equipped with SECCHI instrument (Howard *et al.*, 2008), consisting of *Extreme Ultraviolet Imager* (EUVI; Wuelser *et al.*, 2004) and two inner (COR1, $1.5-4R_{\odot}$) and outer (COR2, $2.5-15R_{\odot}$) white light coronagraphs (Thompson *et al.*, 2003; Howard *et al.*, 2008). White-light heliospheric images are

obtained by the *Heliospheric Imagers* (SECCHI/HI; Eyles *et al.*, 2009). In the following we analyze only the HI1 data, covering the 4° – 24° elongation range, since the studied events in HI2 field of view were too dim and diffuse to be used for sufficiently accurate kinematical measurements or the analysis of the morphological evolution. In the considered period, the separation angle between STEREO-A and STEREO-B was ≈179° in longitude (the separation angles with respect to the Earth were ≈94° and ≈87°, respectively). In the period of interest, the active region AR 11158 rotated from S19W03 to S21W18. Regarding the position of two STEREO spacecraft and location of the active region, the projection effects on the ICME kinematics is negligible.

The kinematical measurements are based on the elongation–time data, $\varepsilon(t)$ for the leading edge of ICMEs. The identification of the corresponding features in images provided by different instruments was accomplished by comparing their morphology and comparing and matching their elongation–time curves (for details of the matching procedure see Maričić *et al.*, 2004). After the corresponding features in EUVI, COR1, COR2, and HI1 images were properly associated, the data for a given feature were joined together, and the elongations were converted to heliocentric distances, R.

The conversion of elongations to radial distances was performed by applying the standard harmonic mean (HM) method, developed by Lugaz (2010); for the application of the HM method see, *e.g.*, Möstl *et al.* (2011), Harrison *et al.* (2012), Rollett *et al.* (2012), and Temmer *et al.* (2012). To check the effects of different conversion-method geometries, we applied also the conversion based on the assumption that the ICME is a relatively thin flux rope that lies in the plane-of-sky (PoS). Thus, the radial distance is defined as $R = D\tan(\varepsilon)$, where D is the Sun–observer distance (hereinafter, the "PoS method"). This geometrical assumption is allowed in this case, since both STEREO spacecraft were in a quadrature position, the CME source region was close to the disk center, and the CME had a flux rope shape. Note that the PoS conversion is analogous to the Fixed-ϕ conversion (Kahler and Webb, 2007; Wood and Howard, 2009) for the propagation direction at the angle of $\phi = 90°$. The results of the HM and PoS methods turned out to be very similar, so that in the following we present mainly the results from the HM method; only comparing them with the outcome of the PoS method when necessary. Finally, at certain points we also apply the drag-based model (DBM; Vršnak *et al.*, 2012) of the heliospheric propagation of ICMEs.

The STEREO coronagraphic data are combined with the SDO soft X-ray data to identify the associated solar flares, since the acceleration phase of a CME is synchronized with its associated flare energy release (Zhang *et al.*, 2001; Maričić *et al.*, 2007; Temmer *et al.* 2008; Temmer, Preiss, and Veronig, 2009; Temmer *et al.*, 2010). The evolution of flares was analyzed using the *Extreme ultraviolet Variability Experiment* (EVE; Woods *et al.*, 2012) onboard the SDO, *i.e.*, the SAM pinhole camera images and the soft X-ray (SXR) flux in the 0.1 – 7 nm channel (http://lasp.colorado.edu/eve/data_access/). In Figure 1a we display the EVE 0.1 – 7 nm SXR flux recorded from 13 February 00:00 to 16 February 24:00, and in Figure 1b we show an example of the SDO SAM pinhole-camera image, capturing the burst that occurred around 05:05 UT on 14 February.

In the period of 13 – 15 February 2011, eight CMEs were launched from the active region AR 11158. They were associated with the bursts marked by arrows in Figure 1a, all occurring in AR 11158. Most of these CMEs were too faint and diffuse to be measured accurately. Thus, we focus our analysis on the three most prominent CMEs, which occurred on 13, 14, and 15 February (hereinafter denoted as 13Feb, 14Feb and 15Feb), and were associated with the strongest three flares in the considered period (see Figure 1a). The eruptions started, as determined from STEREO EUVI images, on 13 February at 17:24 UT, 14 February at 17:06,

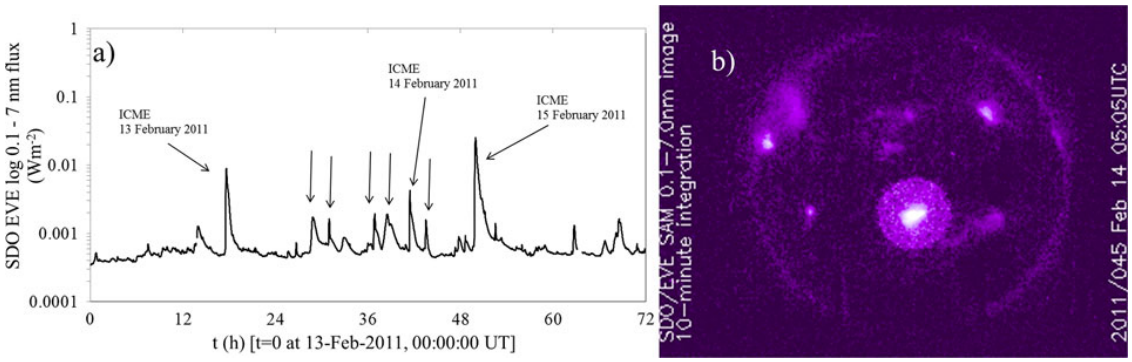

Figure 1 (a) SDO EVE 0.1 – 7 nm SXR flux in the period 13 – 15 February 2011. Arrows mark SXR bursts that occurred in AR 11158 (the bursts associated with the three analyzed CMEs are emphasized). (b) SDO/EVE SAM pinhole camera image, showing the burst that occurred on 14 February at 05:05 UT.

Table 1 Characteristics of the three analyzed CMEs and the associated SXR flares.

Date and start time (UT)	Direction of motion	$v_{\rm m}$ (km s^{-1})	$v_{\rm lp}$ (km s^{-1})	$a_{\rm m}$ (m s^{-2})	$T_{\rm acc}$ (min)	Location	SXR class	$T_{\rm SXR}$ (min)	Δt (min)
13Feb 2011 17:24	W16	550	360	300	55	S20E04	M6.6	10	−26
14Feb 2011 17:06	W12	400	400 (600*)	50	129	S20W04	M2.2	7	−42
15Feb 2011 01:50	W06	1300	600	1400	26	S20W12	X2.2	11	−11

*beyond the distance of $45R_{\odot}$.

and 15 February at 01:50 UT. In the STEREO-COR1 field of view the CMEs appeared at 17:45, 17:45, and 2:05, respectively. The 15Feb CME was associated with a type II radio burst, starting at 01:52 UT (recorded at Culgoora Observatory http://www.ips.gov.au/), *i.e.*, the fastest CME developed a coronal shock.

The initiation of the three analyzed CMEs can be recognized in the EUV images of the low corona (Figure 2), allowing us to measure the eruption kinematics from the early phase of the eruption. General characteristics of CMEs are given in the first six columns of Table 1 (date and UT of the EUV onset, the direction of motion estimated using the HM method, the PoS peak velocity, $v_{\rm m}$, velocity in the late phase of eruption, $v_{\rm lp}$, the peak acceleration, $a_{\rm m}$, and the duration of the acceleration phase, $T_{\rm acc}$). Basic characteristics of the associated flares are given in the next three columns (the flare location, its GOES SXR-class, and the duration of the SXR-burst rise, $T_{\rm SXR}$, *i.e.*, the flare impulsive phase duration). In the last column we show the time lag between the beginning of the CME acceleration phase and the flare onset, Δt, where negative values mean that the SXR burst started after the acceleration-phase onset.

The 13Feb eruption started with the appearance and rise of an arch overlying the active region, which was accompanied by an M6.6 GOES X-ray flare. The CME was first seen in the EUVI STEREO-B image at 17:23:34 UT, at the heliocentric distance of 1.3 solar radii ($R = 1.3R_{\odot}$). During the main acceleration phase, which lasted for approximately 40 min, the CME reached maximum velocity of $v_{\rm m} \approx 550 \pm 50$ km s^{-1} at approximately 17:50 UT. The peak acceleration of $a_{\rm m} \approx 300 \pm 100$ m s^{-2} occurred at the heliocentric distance of

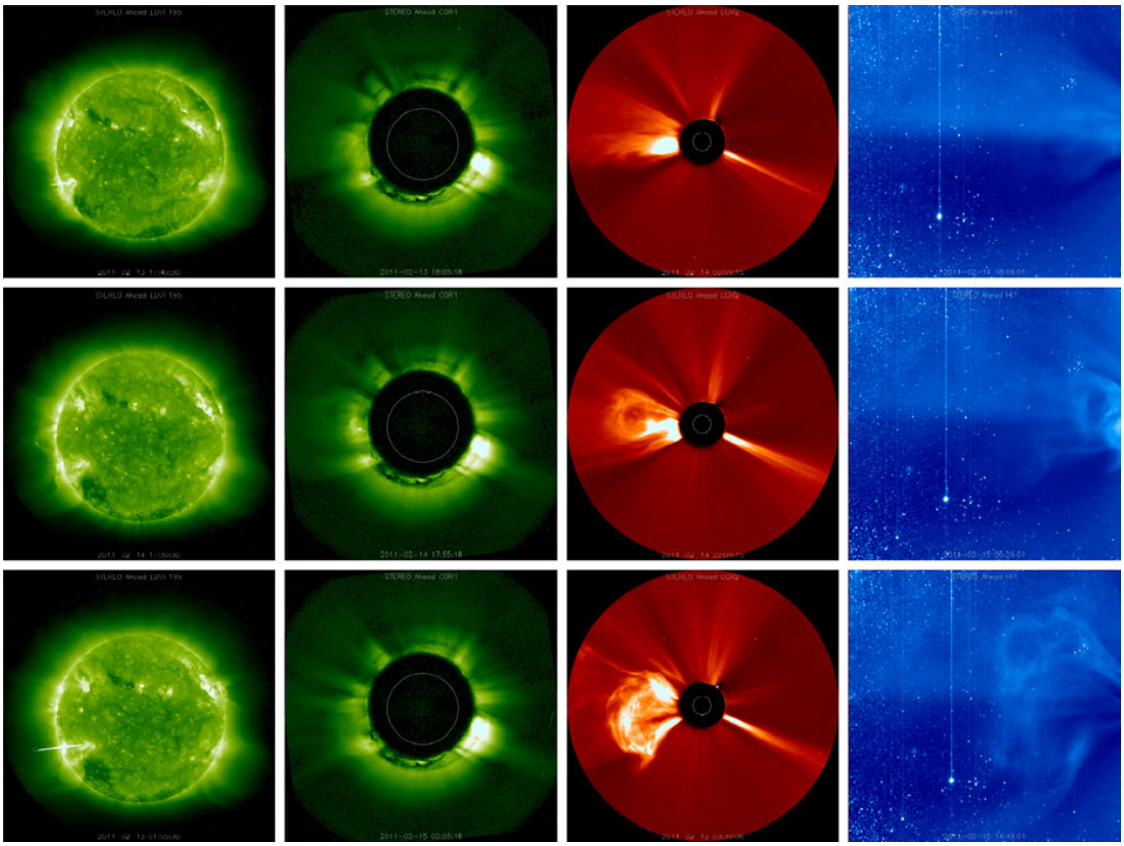

Figure 2 Eruptions of 13 February, 14 February, and 15 February 2011 (top to bottom), captured by the EUVI, COR1, COR2, and HI1 STEREO-A instruments (left to right).

$1.4R_{\odot}$. In the late phase of the eruption, the speed decreased to a roughly constant value of ≈ 360 km s^{-1}.

The 14Feb CME also started by the appearance of an arch overlying the active region. It was first seen in the COR1 STEREO-B image at 16:15:51 UT, at $1.5R_{\odot}$. The main acceleration phase lasted for approximately 2.2 h, providing the peak velocity of $v_{\rm m} \approx 400 \pm 50$ km s^{-1} at approximately 17:20 UT. The peak acceleration of $a_{\rm m} \approx 50 \pm 100$ m s^{-2} occurred at $2.4R_{\odot}$. In the late phase of the eruption, the CME stabilized at the velocity of ≈ 400 km s^{-1}, but after the distance of $\approx 28R_{\odot}$, the velocity suddenly started to increase again, reaching a speed close to 600 km s^{-1} (to be elaborated in Section 3.1).

The 15Feb CME attained a relatively high maximum speed of $v_{\rm m} \approx 1300 \pm 50$ km s^{-1} at the height of $2R_{\odot}$ with maximum acceleration of $a_{\rm m} \approx 1400 \pm 100$ m s^{-2} at a heliocentric distance $1.1R_{\odot}$. After the acceleration phase, which lasted 26 min, it started decelerating and beyond $20R_{\odot}$ the velocity stabilized close to 600 km s^{-1} (to be elaborated in Section 3.1). The overall kinematics of the three events is presented in Figure 3.

To study the characteristics of the ICMEs upon their arrival at the L1 point, we employed the *in situ* data recorded at the *Wind* spacecraft (Lin *et al.*, 1995). We used 1-min averages of the magnetic field strength B, the GSE magnetic field components B_x, B_y, and B_z, the bulk solar-wind speed V, the proton density $N_{\rm p}$, the proton thermal speed $V_{\rm th}$, and the plasma-to-magnetic pressure ratio β, measured by the *Magnetic Field Investigation* (MFI; Lepping *et al.*, 1995) and the *Solar Wind Experiment* (SWE; Ogilvie *et al.*, 1995) available at http://wind.nasa.gov/mfi_swe_plot.php.

For the identification and analysis of the FD event we used the pressure-corrected data from ground-based stations of Space Environmental Viewing and Analysis Network (SE-

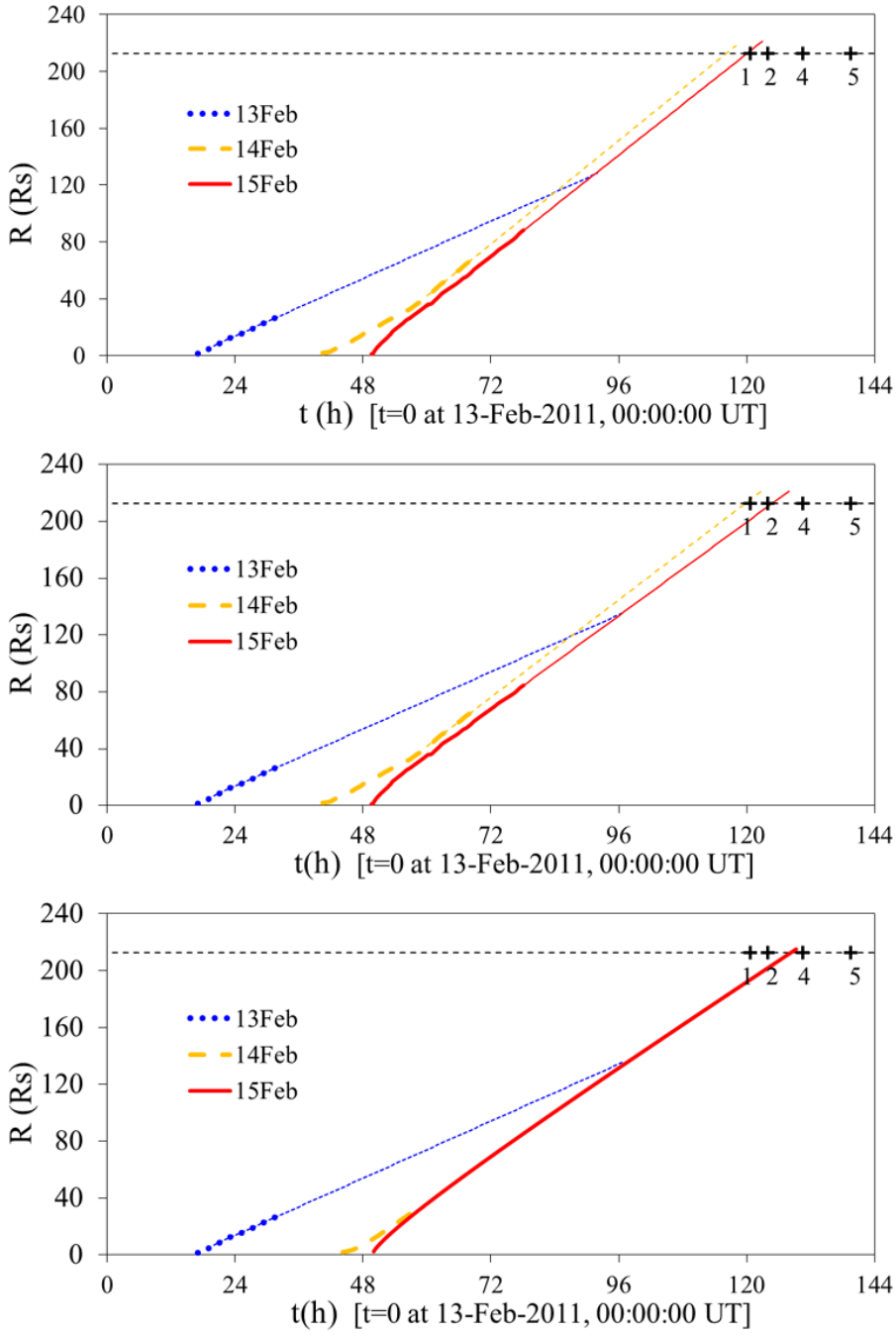

Figure 3 Overall kinematics of the three analyzed ICMEs (symbols are explained in the legend). Thin lines represent the linear-fit extrapolations for the PoS STEREO-A data (top), the HM STEREO-A data (middle), and the DBM Sun-Earth kinematics based on the DBM-parameters inferred from the HM STEREO-A data (bottom; for explanation see Section 3.2). The extrapolations are based on the $R > 10R_{\odot}$ data for 13Feb ICME and the $R > 50R_{\odot}$ data for 15Feb ICME. Horizontal dashed line marks heliocentric distance of the Earth. The beginning of various *in situ* features are marked by pluses (for details see the end of Section 3.2).

VAN) and Moscow neutron monitor (available at http://cr0.izmiran.rssi.ru/mosc/main.htm). SEVAN is a network of multi-particle detectors located at middle to low latitudes. One of its major advantages is probing of different populations of primary cosmic rays that initiate particle cascades in the terrestrial atmosphere. With basic detectors of SEVAN network we simultaneously measure changing fluxes of low energy charged particles (mostly electrons and muons, energy < 100 MeV), high energy muons (energy > 200 MeV) and neutrons

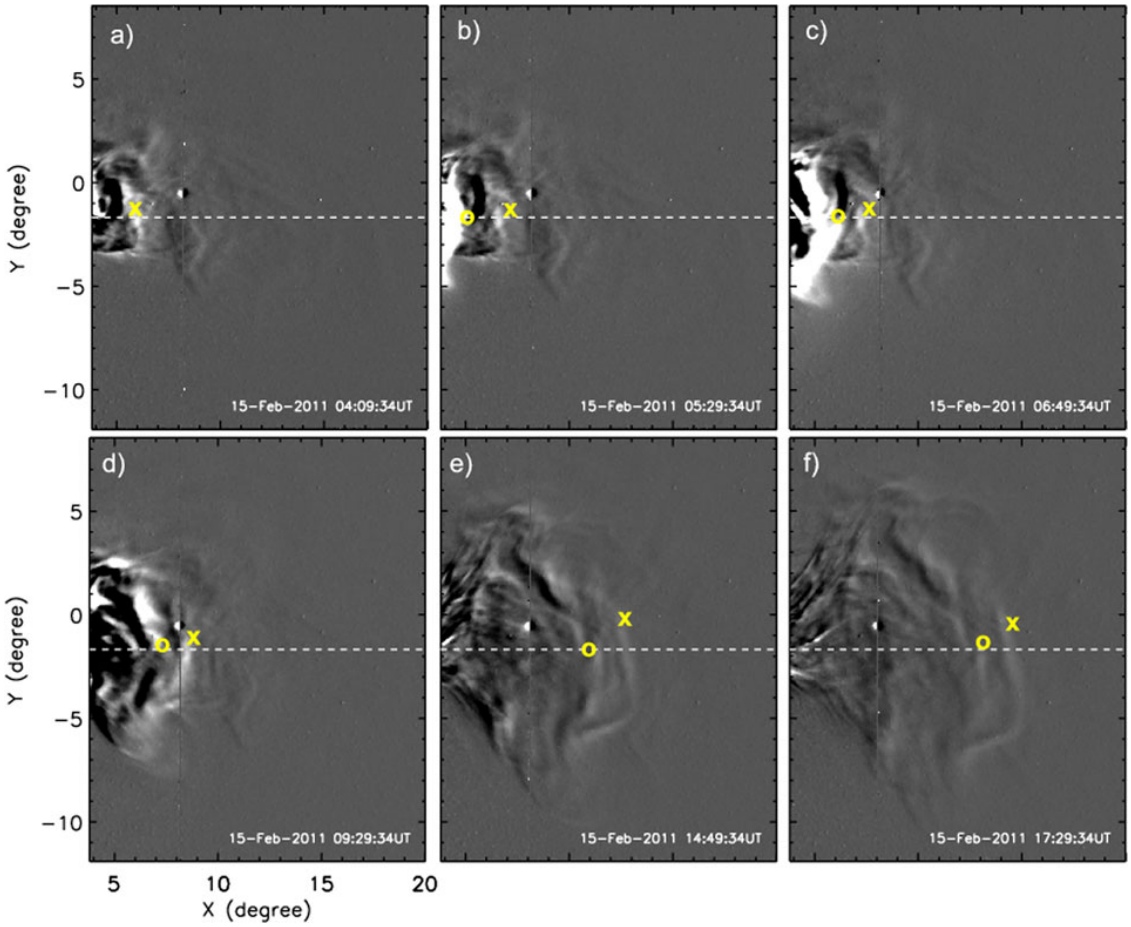

Figure 4 STEREO-B HI1 running-difference images of the 14Feb ICME and 15Feb ICME interaction. The measured leading edge segments of the 14Feb and 15Feb ICMEs are marked by yellow crosses and circles, respectively. The ecliptic plane is indicated by the dashed line.

(Chilingarian *et al.*, 2009). The first SEVAN modules are under test operation at Aragats Space Environmental Center in Armenia, Bulgaria, Croatia, and India. In this analysis we use only the total CR flux data from the Aragats Space Environmental Center and the Zagreb Observatory.

3. Results and Discussion

3.1. Remote Observations

The kinematics of the three analyzed ICMEs (Figure 3), which were launched from the same active region in approximately the same direction (Table 1), indicates that the ICMEs interacted on their way to the Earth, particularly because the last ICME was initially much faster than the preceding two events.

Such a conclusion is supported by the evolution of the 14Feb and 15Feb ICMEs observed in the HI1 field of view. The HI1 images shown in Figure 4 reveal that the 15Feb ICME approached and caught up with the 14Feb ICME (see also the movie at http://stereo-ssc.nascom.nasa.gov/browse/2011/02/15/behind_20110215_hi1_512.mpg) and that in this period the leading edge of the 15Feb ICMEs deformed. In parallel, the velocity of the 14Feb ICME increased, whereas the speed of the 15Feb ICME decreased (Figure 3), supporting the

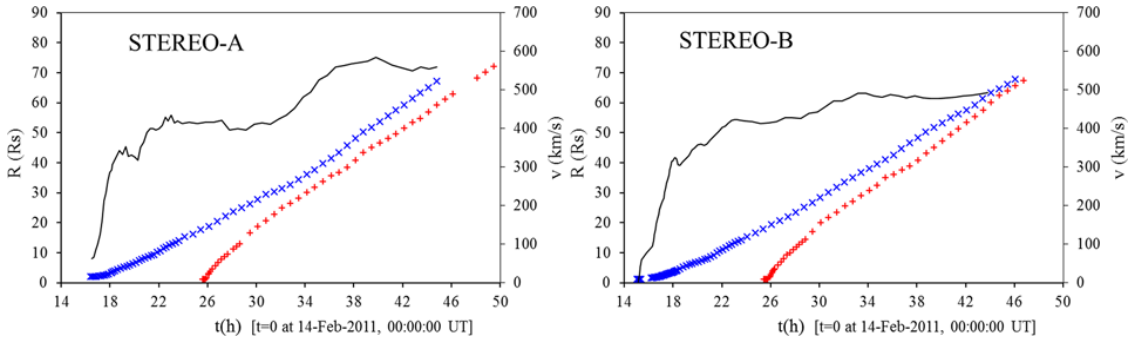

Figure 5 Kinematical $R(t)$ curves for the leading edges of 14Feb ICME and 15Feb ICME (blue crosses and red pluses, respectively), based on STEREO-A (left) and STEREO-B (right) observations. The black curve represents the smoothed $v(t)$ curve of the 14Feb ICME.

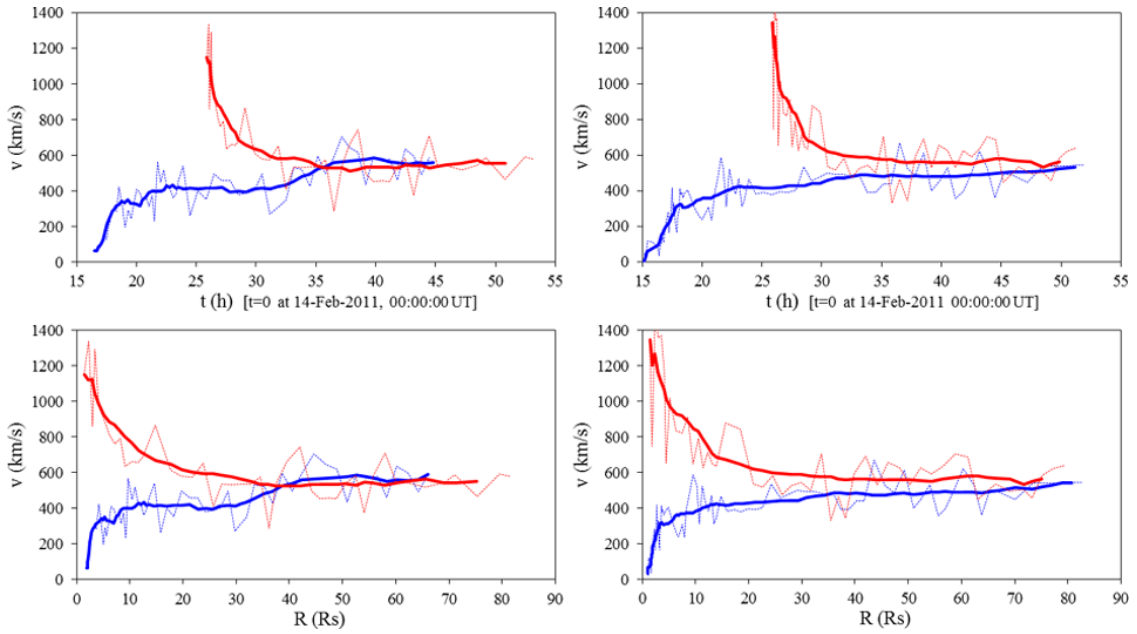

Figure 6 Kinematical curves of the 14Feb and 15Feb ICMEs (lower blue and upper red curves, respectively) for STEREO-A (left) and -B (right). Top: the velocity–time plots; bottom: the velocity–distance plots. Bold lines represent smoothed data.

hypothesis that the two ICMEs interacted. Since the leading edges of both ICMEs were still recognizable after the "collision", it can be concluded that 14Feb ICME was pushed by the 15Feb ICME, rather than being engulfed and assimilated. Therefore, we expect to observe two distinguishable ejection entities at the Earth.

A careful inspection of the HI1 images reveals that the collision between the two ICMEs was not fully symmetric, *i.e.*, one segment of the 15Feb ICME moved more freely, thus being faster than the interacting segment. Since we performed the measurements at the interaction segment, the effect of the interaction can be recognized in the kinematical curves of 14Feb and 15Feb ICMEs (Figures 3, 5, and 6). Kinematical graphs displayed in Figures 3, 5, and 6 reveal that there is a distinct increase of the 14Feb ICME speed in the elapsed-time interval spanning from $t = 32$ h to $t = 37$ h, during which it moved from ≈ 28 to $\approx 45 R_{\odot}$. At the same time, the 15Feb ICME decelerated, and both ICMEs stabilized at the speed of $\approx 500 - 600$ km s^{-1} (Figure 6). Such behavior of the kinematical curves is consistent with the "collision" scenario in which the 15Feb ICME reached the 14Feb ICME and pushed it to

a higher speed, while being decelerated itself. After the momentum transfer was completed, the two ICMEs continued to move together at the same speed, like in an inelastic collision.

Since ICMEs have finite thickness, the interaction of the leading edge of the 15Feb ICME with the trailing edge of the 14Feb ICME must have had started earlier than the effect has arrived at the leading edge of the 14Feb ICME (seen in Figure 5 as the beginning of the speed increase of the leading edge of the 14Feb ICME at the $t \approx 32$ h). In this respect, we note that the deceleration of the 15Feb ICME was initially very rapid, characterized by the peak deceleration of $a_{\mathrm{m}} \approx -400\ \mathrm{m\,s^{-2}}$, which is considerably stronger than usually observed in CMEs of such speed (see, *e.g.*, Figure 1 of Vršnak *et al.*, 2004). As it will be shown later, when the application of the drag-based model is considered, such a deceleration will correspond to a much stronger drag than usually observed (Vršnak *et al.*, 2012). From this point of view, this event is very similar to the ICME–ICME interaction event described by Temmer *et al.* (2012).

Thus, we can assume that the interaction started approximately around the time of the strongest deceleration of the 15Feb CME, *i.e.*, around the elapsed-time $t = 27$ h (see Figure 6, top panel). Since the leading-edge velocity of 14Feb ICME started increasing at $t \approx 32$ h, one finds that the "signal" traveled from the trailing to the leading edge of 14Feb ICME for 5 h. At the beginning of the interaction, the front of 15Feb CME was at the distance of $\approx 5 R_{\odot}$ (Figures 5 and 6), whereas the "signal" arrived to the front of the 14Feb ICME when it was at the distance of $\approx 30 R_{\odot}$ (Figure 6 bottom). Thus, the signal had to travel approximately $25 R_{\odot}$ in 5 h, corresponding to the rest-frame speed of $\approx 1000\ \mathrm{km\,s^{-1}}$. Since the signal was traveled through the 14Feb ICME that was moving before the interaction at the speed of $400\ \mathrm{km\,s^{-1}}$, the relative speed was approximately $600\ \mathrm{km\,s^{-1}}$. Assuming that the signal was carried by magnetohydrodynamical waves, one can estimate that in the considered height-range the Alfvén speed within the 14Feb ICME body was $v_{\mathrm{A}} \approx 600\ \mathrm{km\,s^{-1}}$. As a matter of fact, the "signal", transferring the momentum towards the leading edge of 14Feb ICME, was probably the ICME-driven magnetosonic shock, which also caused the previously mentioned type II burst associated with 15Feb CME. In this respect, it should be mentioned that the shock passage over a CME was already noticed in some previous studies of CME–CME interactions (*e.g.*, Lugaz, Vourlidas, and Roussev, 2009; Liu *et al.*, 2012). Under the shock-passage assumption, the inferred value of the Alfvén speed should be considered as an upper limit, since the shock speed is a product of the Alfvén Mach number and the Alfvén speed.

Finally, we apply the "drag-based model" (DBM; Vršnak and Žic, 2007; Vršnak *et al.*, 2012) to the observed ICME kinematical data. The model is based on the assumption that beyond certain heliocentric distance the propagation of the ICME is governed solely by its interaction with the ambient solar wind (a magnetohydrodynamical version of the aerodynamic drag). In particular, the ICME propagation is determined by the equation of motion which reads $a = -\gamma(v - w)|v - w|$, where a and v are the ICME acceleration and speed, w is the solar-wind speed, and γ is the drag parameter that determines the "efficiency" of the drag. The model was developed primarily for the space weather forecasting purposes (see the online forecasting tool available at http://oh.geof.unizg.hr/CADBM/cadbm.php), but it turned out to be useful in various types of the ICME propagation studies.

In the following we employ the DBM-based least-squares fitting, providing the asymptotic ($R \to \infty$) values of γ and w that provide the best match between the theoretical curve and the observational data. The outcome for the 14Feb and 15Feb ICMEs is presented in Figure 7. Inspecting the displayed graphs, one finds that in both cases the best-fit model curves do not reproduce well the qualitative behavior of the observed data. In the case of the 14Feb ICME, the modeled curves are first above the observed data, and then, beyond

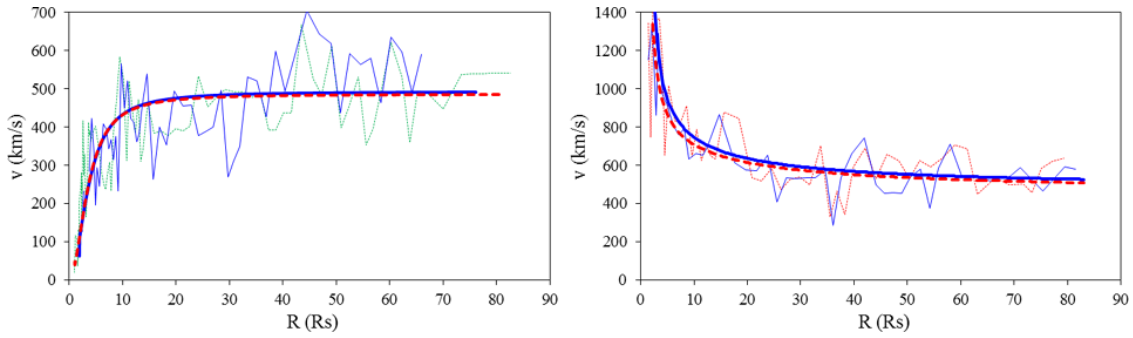

Figure 7 DBM least-squares fit (bold lines) for the 14Feb ICME (left) and 15Feb ICME (right), based on STEREO-A (blue and solid lines) and STEREO-B (red and dashed lines) data.

$R \approx 40R_{\odot}$, it is below the observed data. Such behavior is consistent with the proposed ICME–ICME interaction scenario. In the first phase the slow 14Feb ICME was accelerated by the solar-wind to the speed of ≈ 400 km s^{-1}, and in the second step it was accelerated by the push from the 15Feb ICME to the final speed of $\approx 550-600$ km s^{-1}.

In the case of the 15Feb ICME, the model curves, characterized by $\gamma = 1.4 \times 10^{-7}$ and 1.8×10^{-7} km^{-1} for STEREO-A and -B, reproduce relatively well only the beginning of the deceleration, namely below $\approx 10R_{\odot}$. After that, both model curves show an ongoing deceleration, whereas the observational data show that beyond $\approx 30R_{\odot}$ the speed was approximately constant. This implies that in the first stage, at distances below $30R_{\odot}$ the deceleration should be reproduced by a larger value of γ, whereas beyond that distance γ should be very small. This is again consistent with the ICME–ICME interaction scenario in which the 15Feb CME transfers momentum until reaching the height of $\approx 30R_{\odot}$. when the 14Feb ICME was already at the height of $\approx 40R_{\odot}$.

The presented kinematics is summarized in Figure 3, where we show the extrapolation of the late-phase ICME trajectories and the DBM best-fit trajectory. According to the displayed graphs, the 14Feb/15Feb ICME composite probably hit the 13Feb ICME before reaching the Earth. We roughly estimate that the interaction took place between 125 and $160R_{\odot}$, depending on the method applied.

3.2. *In Situ* Measurements

Guided by the extrapolated trajectories of the analyzed ICME sequence, we associate it with the *in situ* event at L1 that occurred on 18/19 February 2011 (Figure 8; the date is expressed as "day of year", DOY). The *in situ* data displayed in Figure 8 reveal very complex structure of the interplanetary disturbance, consisting of several different segments (separated by vertical dashed lines). The first vertical line marks the shock, as discontinuity is clearly seen throughout the magnetic field and plasma data. It is followed by the region of dense, heated plasma, large magnetic field fluctuations, and enhanced magnetic field, which we identify as the shock sheath region (see, *e.g.*, Burlaga *et al.*, 1984; Richardson and Cane, 2011).

In the second region (hereafter region 2) we find ejection signatures, characterized by elevated magnetic field strength, decreased temperature, very low plasma-to-magnetic field pressure (β), and gradually decreasing flow speed (see *e.g.* Zurbuchen and Richardson, 2006; Richardson and Cane, 2010). We find no clear signature of the magnetic field rotation, except maybe in sub-segments: in the first third of the structure the B_z component changed approximately from -20 nT to $+20$ nT, in the middle third it changed from $+15$ nT to

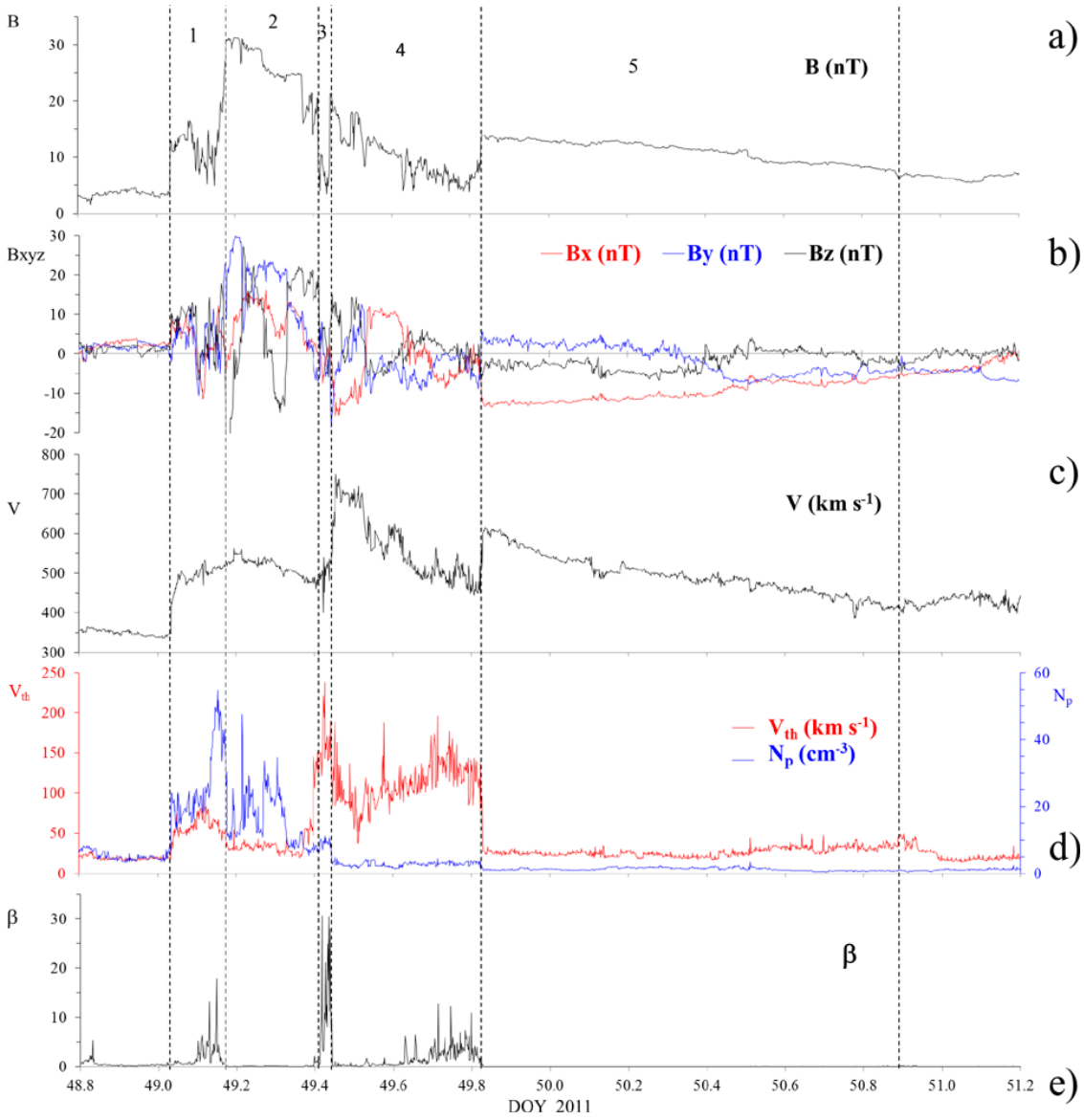

Figure 8 *In situ Wind* measurements at L1 (DOY = 49 is 18 February 2011). (a) the magnetic field strength, (b) GSE magnetic field components, (c) solar-wind speed, (d) proton density and thermal velocity, and (e) plasma-to-magnetic pressure ratio.

-10 nT, whereas in the last third the B_y component changed from $+10$ nT to -10 nT. Note that these sub-structures had very short duration of ≈ 2 h.

Region 3 was characterized by a sharp drop of the magnetic field strength and the increased temperature. The magnetic field strength decreased by a factor of ≈ 2, whereas the temperature increased by a factor of ≈ 4. At the same time, the density increased by a factor of ≈ 1.5 relative to the density in region 2 (upstream of region 3) and by a factor of ≈ 3, relative to region 4 (downstream of region 3), *i.e.*, the overall increase of density was comparable to the decrease of the magnetic field strength. Such a change of parameters resulted in a strong increase of the plasma-to-magnetic pressure ratio β from ≈ 0.2 to ≈ 10, as well as in a drop of the Alfvén speed from ≈ 150 to 50 km s^{-1}. A significant characteristics of region 3 is that one of the magnetic field components (B_x) has opposite orientation on opposite sides of the structure, and that flow velocity becomes turbulent in this period. Finally,

it is important to note that the described changes occur very sharply, *i.e.*, that region 3 was basically bordered by two discontinuities.

Although region 3 had duration of only ≈ 1 h, it certainly represented an independent and well-organized entity. The described changes of the magnetic field and plasma parameters, indicate that this part of the disturbance might represent the reconnection–outflow exhaust (Gosling *et al.*, 2005a, 2005b; Xu, Wei, and Feng, 2011) between two ejections. Namely, according to the 2D reconnection theory put forward by Petschek (1964), when two oppositely directed magnetic fields merge, a pair of slow-mode shocks forms between the inflow and outflow domains, forming a bifurcated current sheet centered at the diffusion region. These shocks are basically switch-off shocks, *i.e.*, the magnetic field component parallel to the current sheet vanishes in the outflow region, where only a weak perpendicular magnetic-field component remains. When a plasma element crosses the shock, it is heated, compressed, and accelerated to the Alfvén speed of the inflow region, becoming a part of the fast reconnection outflow jet (see, *e.g.*, Figure 1 of Vršnak, 1989). In the 2.5D reconnection theory (see, *e.g.*, Skender, Vršnak, and Martinis (2003) and references therein), the situation becomes somewhat more complex, but the basic outcome is the same: plasma in the outflow region is heated and compressed, whereas the magnetic field is weak. In the 2.5D model, the relationships between inflow and outflow parameters depend on the strength of the guide field component, *i.e.*, on the magnetic field shear. Inspecting Figure 2 of Vršnak and Skender (2005), where these relationships are summarized, one finds that for $\beta = 0.1 - 0.5$ at the shear angle of $\Omega_0 \approx 10^\circ$, the outflow-to-inflow ratio equals $\approx 1.7 - 2.3$ for the density, $\approx 2 - 5$ for the temperature, and ≈ 50 for β. Comparing these values with the measured ones, one finds a very good match, thus supporting the interpretation of region 3 in terms of magnetic reconnection. In addition, the 2.5D theory predicts turbulent flows in and around the outflow jet at small Ω_0 (see Section 5.3 of Vršnak and Skender, 2005), again consistent with observations. Yet, it should be noted that a much more meticulous analysis, including detailed analysis of all three components of the magnetic field and velocity (see, *e.g.*, Gosling *et al.*, 2005a, 2005b) would be necessary to justify this *ad hoc* hypothesis. Such an analysis is beyond the scope of this paper, and will be analyzed together with some other similar events in a separate paper (Maričić *et al.*, in preparation).

Region 4 was characterized by high flow speed, low density, and increased temperature. The magnetic field was weaker than in region 2. The value of β was initially low, but increased towards the trailing part of the structure. There was no clear evidence of the overall rotation of the magnetic field within the structure. Possibly, there was a rotation at the beginning of region 4, where the B_y component changed from -10 nT to $+10$ nT over ≈ 3 h, and in the following interval where the B_x component changed from $+10$ nT to -10 nT over ≈ 5 h.

Region 5 started with a sharp increase of the magnetic field and the flow speed, which was accompanied by a steep drop of temperature and the density. To a certain degree it resembled a reverse shock; however, in that case the magnetic field should be increased in between the obstacle and the incoming flow. A detailed inspection of the data in fact shows that although the change was steep, it was not really a shock, since the rise of the magnetic field and flow speed was not smooth, but was jagged. Furthermore, for comparison, let us note that the rise of the forward shock at the beginning of region 1 lasted for less than 2 min, whereas the rise at the beginning of region 5 lasted for $10 - 15$ min.

In region 5, the magnetic field and flow speed were enhanced, gradually decreasing from 14 nT and 600 km s^{-1} at the front, to 7 nT and 420 km s^{-1} at the rear of the structure (the pre-event values were 3 nT and 350 km s^{-1}, respectively). The plasma-to-magnetic pressure ratio within region 5 was very low, as were the density and temperature. The B_y and B_z

Table 2 Expected ICME arrival times compared to the *in situ* onset times and the CR data.

Expected arrival time for 15Feb ICME		
STEREO-A/PoS	DOY 49.01	00:20 UT 18 February 2011
STEREO-B/PoS	DOY 48.91	21:45 UT 17 February 2011
STEREO-A/HM	DOY 49.20	04:55 UT 18 February 2011
STEREO-B/HM	DOY 49.06	01:30 UT 18 February 2011
STEREO-A/DBM	DOY 49.34	08:12 UT 18 February 2011
STEREO-B/DBM	DOY 49.23	05:24 UT 18 February 2011
In situ onset times		
Wind shock	DOY 49.03	00:30 UT 18 February 2011
Wind 13Feb ICME	DOY 49.17	04:04 UT 18 February 2011
Wind 14Feb ICME	DOY 49.44	10:33 UT 18 February 2011
Wind 15Feb ICME	DOY 49.82	19:40 UT 18 February 2011
Forbush decrease		
FD onset	DOY 49.05	01:10 UT 18 February 2011
FD minimum	DOY 49.56	13:30 UT 18 February 2011
FD end	DOY 53.70	17:00 UT 22 February 2011

magnetic field components were anti-correlated, where B_y changed from $+4$ to -7 nT and B_z simultaneously changed from -5 to $+2$ nT, indicating a possible rotation of the magnetic field. These properties indicate that the region-5 structure might be a magnetic cloud. The structure ahead of it (region 4) was compressed and overheated (see Figure 8d), since it was sandwiched between the slower region-2 disturbance and the incoming region-5 structure. Seemingly, the region-4 volume reacted by an overexpansion, which led to the increase of the flow speed at the front of region 4 to 730 km s^{-1}, and the decrease to 470 km s^{-1} at its trailing edge. Furthermore, such expansion could be a driver of the reconnection at the interface between region 2 and 4.

Finally, we compare the starting times of the *in situ* disturbances that we attributed to the 13Feb, 14Feb, and 15Feb ICMEs, with the expected arrival times that are based on the extrapolation of the remotely measured late-phase ICME data. The outcome is visualized in Figure 3, where we mark the shock passage and the start times of the described *in situ* disturbances (regions 2, 4, and 5). Inspecting the displayed graphs one finds that the direct extrapolation of the remote measurements "predicts" the arrivals too early. For example, the HM-data for 14Feb ICME map approximately to the *in situ* shock (see the middle panel of Figure 3), or more precisely, the ICME arrived 11 h later than expected (the actual arrival is marked by "4"). The difference is even larger for the PoS data (Figure 3, top panel). Bearing in mind that 13Feb ICME had a certain thickness, and that there was an offset between the shock and the leading edge of the disturbance, a forecaster who would use the remote data would also predict the shock arrival too early for some ten hours.

The differences for the 15Feb ICME are presented in more detail in Table 2. The ICME arrived around 20 h later than "predicted" by the PoS data, and the corresponding difference for the HM data is 15 – 18 h. Somewhat better is the best-fit estimate from DBM/HM-data (see Figure 3 bottom), predicting the arrival 11 – 14 h too early (see Table 2).

An explanation for such delays would be a deceleration of the ICME complex, being even stronger than inferred by DBM. However, in that case one would expect the ICME *in situ* speed to be considerably lower than recorded. The only way to avoid the inconsistency is that the Earth was not hit by the apex part of the ICME, but rather with a flank segment,

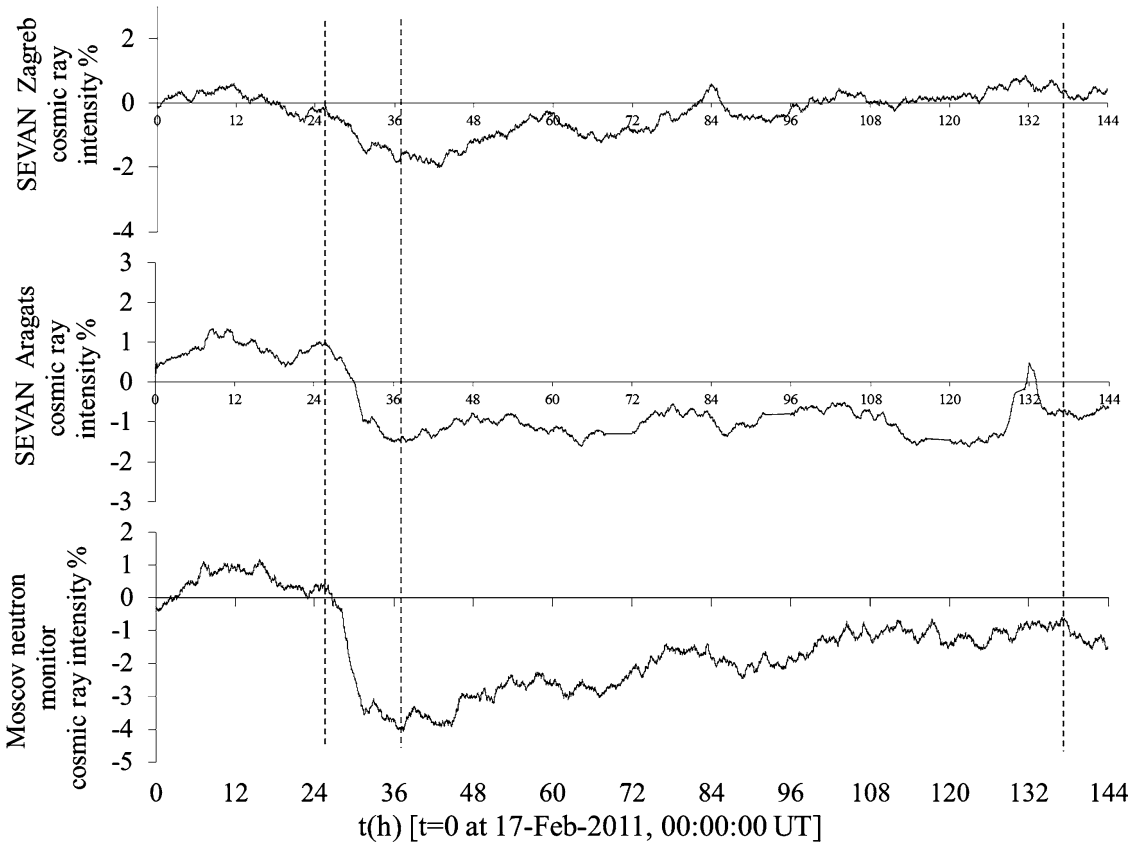

Figure 9 CR count-rate curves from (a) SEVAN-Zagreb, (b) SEVAN-Aragats, and (c) Moscow neutron monitor. The onset, the minimum, and the end of FD are marked by vertical lines.

which is expected to arrive later due to the leading edge curvature. This might also explain the lack of the magnetic cloud signatures in the magnetic field *in situ* data (Möstl *et al.*, 2010).

3.3. Forbush Decrease

Finally, we analyze the CR data, recorded by three instruments: SEVAN-Zagreb, SEVAN-Aragats, and Moscow neutron monitor (NM) station. The pressure-corrected hourly averaged CR count-rates were set relative to the average value in the four-day pre-FD period, to emphasize relative changes in the CR flux. The data are presented in Figure 9, where the FD onset, minimum, and the end are marked by vertical lines (for specific values see Table 2). Let us note that the FD might have started earlier on global scale, since the measurements were hampered by the CR daily variation. Inspecting Table 2 one finds that the estimated FD onset time is basically simultaneous with the shock arrival at the Earth, if extrapolated from its arrival at the *Wind* satellite. The shape of FD was asymmetric, as expected for depressions caused by ICMEs; however, a typical shock-related two-step structure was not clearly seen.

We estimate the end of the depression $\approx$4 days after the passage of the solar wind disturbance over the Earth, where the CR count-rate reached a more or less constant value (neglecting the daily variations), but it did not return to the pre-decrease levels. This indicates prolonged influence of the so called “shadow effect”, where the disturbance still shields the observer from incoming CRs, casting a gradually weakening shadow as it propagates away

and is presumably connected to the size of the disturbance (see, *e.g.*, Lockwood, Webber, and Jokipii, 1986; Dumbović *et al.*, 2011).

There were no visible substructures within the CR depression, suggesting that the observed complex *in situ* event had similar effect on CRs as a single ICME would have, although we cannot neglect the possibility that small substructures in the depression were masked by daily variations. We roughly estimate the amplitude of the depression to be ≈ 4 % for Moscow NM (daily variations possibly adding $\approx \pm 0.5$ %), which is close to average (*e.g.*, Dumbović *et al.*, 2011), or slightly above average (*e.g.*, Richardson and Cane, 2011), value for ground-based observations.

The fact that the ICME was not geoeffective (Kane, 2011a), causing only Dst ≈ -30 nT, is in agreement with the observed "under-recovery" (*i.e.*, CR count-rate did not return to the pre-increase level), confirming that the change in the geomagnetic field can indeed play a role in the FD recovery, as suggested by Chilingarian and Bostanjyan (2010), and discussed by Dumbović *et al.* (2012) regarding the so called "branching effect". The branching effect concerns the observed twofold dependence of FD magnitude, |FD|, on the disturbance magnetic field strength, B (for more details see Dumbović *et al.* 2011, 2012). By its characteristics, |FD| ≈ 4 % at $B \approx 25$ nT, the event belonged to the population mostly involving geoeffective events, *i.e.*, to the "lower branch" of the |FD|(B) relationship (smaller |FD| for same B). This confirms that geoeffectiveness itself cannot explain branching of the |FD|(B) relationship, as concluded by Dumbović *et al.* (2012).

4. Summary and Conclusions

Remote satellite data recorded by STEREO and SDO spacecraft were used to investigate the kinematical evolution of three Earth-directed ICMEs, launched from the active region AR 11158 within 1.4-day interval. Two of them interacted in the STEREO-HI1 field of view, providing detailed observation of an ICME–ICME interaction. From the morphology and kinematical data we conclude that the two ICMEs "collided" and continued propagating bound together, but still being distinguishable as two separate entities.

Extrapolating the kinematics of this ICME complex, we infer that it would reach and presumably interact with another ICME, as it was launched from the same active region and propagated in the same direction. Furthermore, from the extrapolation we derive an approximate arrival time at the L1 point and associate these events with the complex ICME event recorded by the *in situ* measurements. We find that the three ICMEs identified at L1 match the three ICMEs observed in HI1, where the first two ICMEs partly merged by magnetic reconnection at their interface. We found a difference between the expected and actual arrival time of ICMEs, which we explain by the flank-impact.

The three ICMEs produced a single FD event, as recorded by ground-based detectors. The shape and magnitude of the FD corresponded to a typical ICME-produced CR depression, and did not contain any substructures corresponding to individual ICMEs involved. From the CR point of view, the three ICMEs were seen as a single large-size structure, which prolonged the CR recovery.

Acknowledgements The authors are grateful to the STEREO/SECCHI team (Goddard Space Flight Center, Naval Research Laboratory), the SOHO/LASCO team (Naval Research Laboratory, Max Planck Institute for Solar System Research), the *Wind* team, the Moscow neutron monitor team, SEVAN Cosmic Ray Division for providing the data and MT gratefully acknowledges the Austrian Science Fund (FWF): V195-N16. The research leading to these results has received funding from the European Commission's Seventh Framework Programme (FP7/2007–2013) under the grant agreements n° 263252 [COMESEP] and n° 284461 [eHEROES].

References

Burlaga, L.F., McDonald, F.B., Ness, N.F., Schwenn, R., Lazuras, A.J., Mariani, F.: 1984, *J. Geophys. Res.* **89**, 6579 – 6587.

Cane, H.V.: 2000, *Space Sci. Rev.* **93**, 55 – 77.

Chilingarian, A., Bostanjyan, N.: 2010, *Adv. Space Res.* **45**, 614 – 621.

Chilingarian, A., Angelov, Ch., Arakelyan, K., Arsov, T., Avakyan, K., Chilingaryan, S., *et al.*: 2009, In: *Proc. 31st Int. Cosmic Ray Conf.*, icrc0681LODZ.

Dumbović, M., Vršnak, B., Čalogović, J., Karlica, M.: 2011, *Astron. Astrophys.* **531**, A91.

Dumbović, M., Vršnak, B., Čalogović, J., Župan, R.: 2012, *Astron. Astrophys.* **538**, A28.

Eyles, C.J., Harrison, R.A., Davis, C.J., *et al.*: 2009, *Solar Phys.* **254**, 387.

Forbush, S.E.: 1937, *Phys. Rev.* **51**, 1108 – 1109.

Gopalswamy, N., Yashiro, S., Kaiser, M.L., Howard, R.A., Bougeret, J.L.: 2001, *Astrophys. J. Lett.* **548**, L91 – L94.

Gosling, J.T., Skoug, R.M., McComas, D.J., Smith, C.W.: 2005a, *J. Geophys. Res.* **110**, A01107.

Gosling, J.T., Skoug, R.M., McComas, D.J., Smith, C.W.: 2005b, *Geophys. Res. Lett.* **32**, L05105.

Harrison, R.A., Davies, J.A., Möstl, C., Liu, Y., Temmer, M., Bisi, M.M., *et al.*: 2012, *Astrophys. J.* **750**, 45.

Hess, V.F., Demmelmair, A.: 1937, *Nature* **140**, 316 – 317.

Howard, R.A., Moses, J.D., Vourlidas, A., Newmark, J.S., Socker, D.G., Plunkett, S.P., *et al.*: 2008, *Space Sci. Rev.* **136**, 67 – 115.

Kahler, S.W., Webb, D.F.: 2007, *J. Geophys. Res.* **112**, 9103.

Kaiser, M.L., Kucera, T.A., Davila, J.M., St. Cyr, O.C., Guhathakurta, M., Christian, E.: 2008, *Space Sci. Rev.* **136**, 5 – 16.

Kane, R.P.: 2011a, *Indian J. Radio Space Phys.* **40**, 253 – 256.

Kane, R.P.: 2011b, *Indian J. Radio Space Phys.* **40**, 297 – 300.

Kane, R.P.: 2012, *Indian J. Radio Space Phys.* **41**, 520 – 523.

Lepping, R.P., Acuna, M.H., Burlaga, L.F., Farrell, W.M., Slavin, J.A., Schatten, K.H., *et al.*: 1995, *Space Sci. Rev.* **71**, 207 – 229.

Lin, R.P., Anderson, K.A., Ashford, S., Carlson, C., Curtis, D., Ergun, R., *et al.*: 1995, *Space Sci. Rev.* **71**, 125 – 153.

Liu, Y.D., Luhmann, J.G., Möstl, C., Martinez-Oliveros, J.C., Bale, S.D., Lin, R.P., Harrison, R.A., Temmer, M., Webb, D.F., Odstrcil, D.: 2012, *Astrophys. J. Lett.* **746**, L15.

Lockwood, J.A.: 1971, *Space Sci. Rev.* **12**, 658 – 715.

Lockwood, J.A., Webber, W.R., Jokipii, J.R.: 1986, *J. Geophys. Res.* **91**, 2851 – 2857.

Lugaz, N.: 2010, *Solar Phys.* **267**, 411 – 429.

Lugaz, N., Vourlidas, A., Roussev, I.I.: 2009, *Ann. Geophys.* **27**, 3479 – 3488.

Maričić, D., Vršnak, B., Stanger, A.L., Veronig, A.: 2004, *Solar Phys.* **225**, 337 – 353.

Maričić, D., Vršnak, B., Stanger, A.L., Veronig, A.M., Temmer, M., Roša, D.: 2007, *Solar Phys.* **241**, 99 – 112.

Möstl, C., Temmer, M., Rollett, T., Farrugia, C.J., Liu, Y., Veronig, A.M., Leitner, M., Galvin, A.B., Biernat, H.K.: 2010, *Geophys. Res. Lett.* **37**, L24103.

Möstl, C., Rollett, T., Lugaz, N., Farrugia, C.J., Davies, J.A., Temmer, M., *et al.*: 2011, *Astrophys. J.* **741**, 34.

Ogilvie, K.W., Chornay, D.J., Fritzenreiter, R.J., Hunsaker, F., Keller, J., Lobell, J.: 1995, *Space Sci. Rev.* **71**, 55 – 77.

Oh, S.Y., Yi, Y.: 2012, *Solar Phys.* **280**, 197 – 204.

Pesnell, W.D., Thompson, B.J., Chamberlin, P.C.: 2012, *Solar Phys.* **275**, 3 – 15.

Petschek, H.E.: 1964, In: Hess, W.N. (ed.) *AAS-NASA Symposium on the Physics of Solar Flares*, *NASA SP-50*, 425 – 438.

Richardson, I.G.: 2004, *Space Sci. Rev.* **111**, 267 – 376.

Richardson, I.G., Cane, H.V.: 2010, *Solar Phys.* **264**, 189 – 237.

Richardson, I.G., Cane, H.V.: 2011, *Solar Phys.* **270**, 609 – 627.

Rollett, T., Möstl, C., Temmer, M., Veronig, A.M., Farrugia, C.J., Biernat, H.K.: 2012, *Solar Phys.* **276**, 293 – 314.

Schrijver, C.J., Aulanier, G., Title, A.M., Paria, E., Delannee, C.: 2011, *Astrophys. J.* **738**, 167.

Shen, F., Wu, S.T., Feng, X., Wu, C.: 2012, *J. Geophys. Res.* **117**, A11101.

Simpson, J.A.: 1954, *Phys. Rev.* **94**, 426 – 440.

Skender, M., Vršnak, B., Martinis, M.: 2003, *Phys. Rev. E* **68**, 046405.

Temmer, M., Preiss, S., Veronig, A.M.: 2009, *Solar Phys.* **256**, 183 – 199.

Temmer, M., Veronig, A.M., Vršnak, B., Rybák, J., Gömöry, P., Stoiser, S., Maričić, D.: 2008, *Astrophys. J. Lett.* **673**, L95 – L98.

Temmer, M., Veronig, A.M., Kontar, E.P., Krucker, S., Vršnak, B.: 2010, *Astrophys. J.* **712**, 1410 – 1420.

Temmer, M., Vršnak, B., Rollett, T., Bein, B., de Koning, C.A., Liu, Y., *et al.*: 2012, *Astrophys. J.* **749**, 57.
Thompson, W.T., Davila, J.M., Fisher, R.R., Orwig, L.E., Mentzell, J.E., Hetherington, S.E., *et al.*: 2003, In: Keil, S.L., Avakyan, S.V. (eds.) *Innovative Telescopes and Instrumentation for Solar Astrophysics*, *Proc. SPIE* **4853**, 1 – 11.
Vršnak, B.: 1989, *Solar Phys.* **120**, 79 – 92.
Vršnak, B., Skender, M.: 2005, *Solar Phys.* **226**, 97 – 199.
Vršnak, B., Žic, T.: 2007, *Astron. Astrophys.* **472**, 934 – 937.
Vršnak, B., Ruždjak, D., Sudar, D., Gopalswamy, N.: 2004, *Astron. Astrophys.* **423**, 717 – 728.
Vršnak, B., Žic, T., Vrbanec, D., Temmer, M., Rollett, T., Möstl, C., *et al.*: 2012, *Solar Phys.* doi:10.1007/s11207-012-0035-4.
Wang, Y.M., Ye, P.Z., Wang, S., Zhou, G.P., Wang, J.X.: 2002, *J. Geophys. Res.* **107**, 1340.
Wood, B.E., Howard, R.A.: 2009, *Astrophys. J.* **702**, 901.
Woods, T.N., Eparvier, F.G., Hock, R., Jones, A.R., Woodraska, D., Judge, D., *et al.*: 2012, *Solar Phys.* **275**, 115 – 143.
Wuelser, J., Lemen, J.R., Tarbell, T.D., *et al.*: 2004, In: Fineschi, S., Gummin, M.A. (eds.) *Telescopes and Instrumentation for Solar Astrophysics*, *Proc. SPIE* **5171**, 111 – 122.
Xu, X., Wei, F., Feng, X.: 2011, *J. Geophys. Res.* **116**, A05105.
Zhang, J., Dere, K.P., Howard, R.A., Kundu, M.R., White, S.M.: 2001, *Astrophys. J.* **559**, 452 – 462.
Zurbuchen, T.H., Richardson, I.G.: 2006, *Space Sci. Rev.* **123**, 31 – 43.